J. Fluid Mech. (2007), *vol.* 575, *pp.* 1–26.
doi:10.1017/S0022112006003776 Printed in the United Kingdom

Dynamics and noise emission of vortex cavitation bubbles

JAEHYUG CHOI AND STEVEN L. CECCIO

Department of Mechanical Engineering, The University of Michigan, Ann Arbor, MI 48109-2121, USA

(Received 17 July 2005 and in revised form 7 August 2006)

The growth and collapse of a cavitation bubble forming within the core of a line vortex was examined experimentally to determine how the dynamics and noise emission of the elongated cavitation bubble is influenced by the underlying non-cavitating vortex properties. A steady line vortex was formed downstream of a hydrofoil mounted in the test section of a recirculating water channel. A focused pulse of laser light was used to initiate a nucleus in the core of a vortex, allowing for the detailed examination of the growth, splitting and collapse of individual cavitation bubbles as they experience a reduction and recovery of the local static pressure. Images of single-bubble dynamics were captured with two pulse-synchronized high-speed video cameras. The shape and dynamics of single vortex cavitation bubbles are compared to the original vortex properties and the local static pressure in the vortex core, and an analysis was performed to understand the relationship between the non-cavitating vortex properties and the diameter of the elongated cavitation bubble. Acoustic emissions from the bubbles were detected during growing, splitting and collapse, revealing that the acoustic impulse created during collapse was four orders of magnitude higher than the noise emission due to growth and splitting. The dynamics and noise generation of the elongated bubbles are compared to that of spherical cavitation bubbles in quiescent flow. These data indicate that the core size and circulation are insufficient to scale the developed vortex cavitation. The non-cavitating vortex circulation and core size are not sufficient to scale the bubble dynamics, even though the single-phase pressure field is uniquely scaled by these parameters. A simple analytical model of the equilibrium state of the elongated cavitation bubble suggests that there are multiple possible equilibrium values of the elongated bubble radius, each with varying tangential velocities at the bubble interface. Thus, the details of the bubble dynamics and bubble–flow interactions will set the final bubble dimensions.

1. Introduction

The dynamics and acoustics of spherical cavitation bubbles have been examined by many workers and are well understood (Brennen 1995; Leighton, Ho & Flaxman 1997). The growth, collapse and noise emission of non-spherical bubbles have also been studied, but to a much lesser degree. Deformation of a collapsing cavitation bubble can lead to significant reduction in the emitted noise the bubble produces compared to the noise emitted by nearly spherical bubbles. This phenomenon has been examined for hydrodynamic travelling bubble cavitation (Ceccio & Brennen 1991; Kumar & Brennen 1993; Kuhn de Chizelle, Ceccio & Brennen 1995; Li & Ceccio 1996), and for laser induced cavitation bubbles (Vogel & Lauterborn 1988; Oweis, Choi & Ceccio 2004). In many cases, consideration of spherical bubble dynamics can

be used to scale the noise produced by non-spherical bubbles when they are deformed but maintain aspect ratios close to unity. The acoustic impulse generated by such bubbles can be scaled with the bubble maximum volume and the liquid pressure surrounding the bubble during collapse. However, if the bubbles are significantly deformed, the noise produced upon collapse can be negligible, since the bubble may be highly sheared, or undergo fission, and thus not achieve significant volume accelerations (Brennen 2002). In these extreme cases, traditional scaling methods based on spherical bubble dynamics significantly over-predict the noise produced by the collapsing bubble.

Single highly non-spherical cavitation bubbles can form in the low-pressure core region of strong vortices. Many workers have studied vortex cavitation, and a review is provided by Arndt (2002). Vortex cavitation often occurs in the concentrated vortices formed in the tip region of lifting surface or in vortices present in the turbulent flow field associated with jets and shear layers (see, for example, O'Hern 1990; Belahadji, Franc & Michel 1995; Maines & Arndt 1997; Gopalan, Katz & Knio 1999). Typically, a small nucleus is present within or captured by the vortex (Oweis *et al.* 2005). If the pressure in the vortex core falls below the liquid vapour pressure, the critical tension of the nucleus can be reached, resulting in a growing vapour bubble. The bubble will expand to a fraction of the vortex core size in the radial direction and then continue to grow along the vortex axis. An increase in the static pressure near the bubble will cause the elongated cavitation bubble to collapse, often leading to the production of an acoustic pulse. In fact, engineers define the point of vortex cavitation inception to be when these acoustic pulses are first discernable.

The scaling of vortex cavitation inception with varying nuclei distributions and Reynolds numbers has received considerable attention (Maines & Arndt 1997; Astolfi, Fruman & Billard 1999). Scaling of developed vortex cavitation and its resulting noise is also a challenge (Hsiao & Chahine 2005). The relationship between the non-cavitating vortical flow field and the resulting cavitation bubble dynamics can be complex, and prediction of cavitation event rates and noise-production is influenced by the process of bubble elongation and splitting. Elongated bubbles can break into several smaller sub-bubbles before the first collapse, and this fission process can lead to multiple acoustic emissions from the collapse of a single elongated bubble (Choi & Chahine 2004; Hsiao & Chahine 2005). The resulting acoustic impulse frequency spectra and intensity of the noise produced by the collapse may not be predicted easily.

Experimental observations of naturally occurring vortex cavitation bubbles are made difficult by the stochastic nature of vortex cavitation. It can be difficult to know where the bubble will first occur in the vortical flow. Arndt & Maines (2000) employed both high-speed movies and single-image flash photography to capture detailed images of naturally occurring vortex cavitation. The camera flash was triggered as individual cavitation bubbles intersected a laser beam placed in the region of expected bubble formation. Another method of studying the details of cavitation bubble dynamics is the formation of a nucleus by a spark or focused light-source with synchronized image-capturing devices to observe the bubble or bubbles. The use of a light pulse for nuclei formation is advantageous for the study of vortex cavitation since the light will not disturb the underlying flow. Oweis *et al.* (2004) measured the noise pulse and spectra associated with single laser-induced cavitation bubble events as they occur within the core of a vortex. The energy deposited was sufficient to cause the growth of a cavitation bubble even when the pressure in the vortex core was above vapour pressure. The rapid growth and collapse of individual cavitation bubbles was observed, and the noise produced by the collapsing bubbles was successfully scaled with spherical bubble dynamics when the bubbles were not highly deformed.

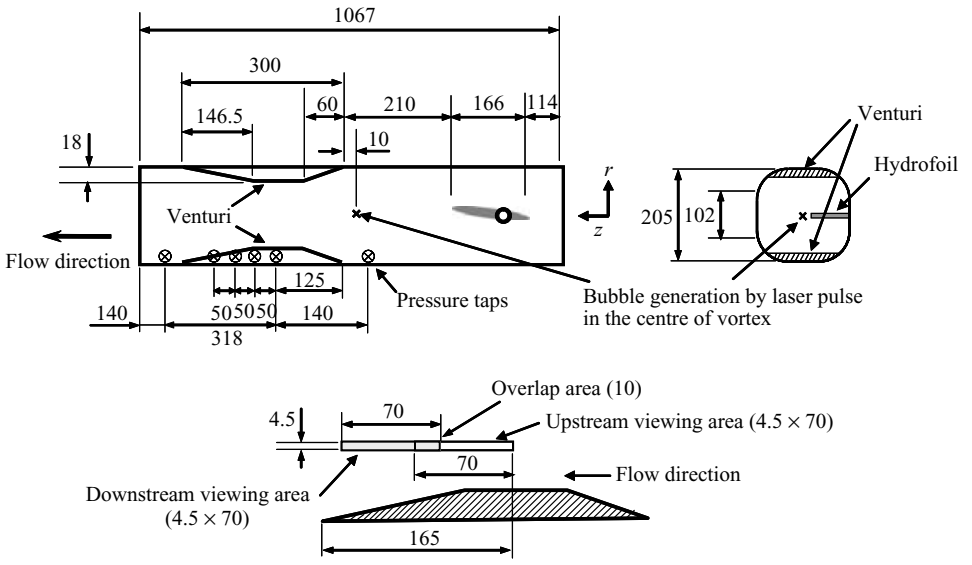

FIGURE 1. Schematic diagram of the Venturi in the water tunnel test section; the location of the hydrofoil and the laser-induced bubble are also illustrated. The fields-of-view of the two high-speed cameras are shown. Dimensions are in mm.

In the present work, we produce elongated bubbles experimentally in the core of concentrated vortices and examine their growth, splitting and collapse. Our goals are two-fold: (i) we wish to examine how the non-cavitating vortex properties influence the inception and dynamics of the single vortex cavitation bubbles and (ii) we wish to examine how these dynamics lead to the production of noise.

Detailed measurements are achieved by initiating a small nucleus in the vortex core with a focused pulse of laser light (see figure 1). A vortex is formed downstream of a hydrofoil, and the vortex passes through a contraction in order to achieve a reduction and recovery in overall pressure. A nucleus is created well upstream of the inception point. The small bubble convects into the low-pressure region where inception occurs. The bubble then grows along the axis of the vortex until it convects into the region of pressure recovery where it will collapse. Observation of the bubble dynamics is accompanied by the measurement of the noise emitted by the bubble.

With this data, we examine how variation in free-stream conditions and vortex properties influence the bubble dynamics and noise production, including the process of bubble fission. Ideally, the characteristics of the non-cavitating vortical flow can be used to scale the dynamics of the individual cavitation bubbles, although we will show below that this is not the case. We also explore how the growth, fission and collapse of the bubbles can lead to the creation of an acoustic pulse, and we will compare the noise produced by the deformed cavitation bubble with that produced by the collapse of near-spherical bubbles.

2. Experimental set-up

2.1. *Flow facility and set-up*

The University of Michigan 9 in. water tunnel was used to conduct these experiments. The tunnel has a circular contraction downstream of a series of flow management screens with area contraction ratio 6.4:1. The test section has a 22.9 cm (9 in.) diameter round inlet that is then faired into a rectangular test section with widely rounded

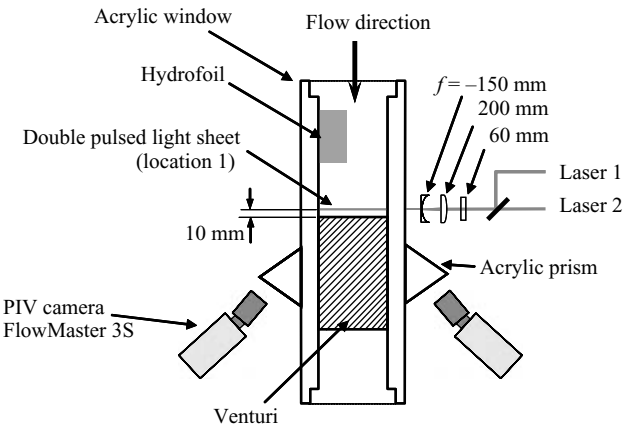

FIGURE 2. A schematic plan view of the test section with the stereo PIV set-up. The light sheet making optics, prisms and cameras with Scheimpflug lens mounts are shown. Light sheet location 1 was 10 mm upstream of the Venturi inlet, and location 2 was 110 mm downstream (not shown).

corners. The maximum test-section inlet flow velocity is $18\,\mathrm{m\,s^{-1}}$, and the test section static pressure can be varied from near vacuum up to 200 kPa. The tunnel holds $3.8\,\mathrm{m^3}$ (1000 US gallons) of water that can be deaerated to 10 % saturation at atmospheric pressure. Further details regarding the water tunnel are reported in Oweis *et al.* (2004).

A vortical flow is created using a cambered hydrofoil with a non-standard cross-section mounted to one window of the test section. The hydrofoil has a rectangular platform of 9.5 cm span and 16.6 cm chord with a rounded tip. Two hydrofoils were manufactured and then modified in the following ways: a wire was attached along the chord near the tip, and the suction side of one hydrofoil was roughened. The incident flow angle was varied from 4.0° to 4.5° to vary the vortex circulation and core size. Vortices are formed and shed near the hydrofoil tip, and these vortices merge to form a single vortex within half a chord length downstream of the trailing edge. A Venturi section (figure 1) was mounted 21 cm downstream of the trailing edge to produce a reduction and recovery of the flow static pressure. The area of the test section upstream of the Venturi is $0.0378\,\mathrm{m^2}$ and reaches a minimum of $0.0331\,\mathrm{m^2}$ at the Venturi throat, yielding an area reduction of 12 %. Four acrylic windows permit optical access to the test section flow.

Measurements of vortex cavitation were undertaken with free-stream velocities U_∞ in the range of 9.7 to $10.3\,\mathrm{m\,s^{-1}}$ and a variety of static pressures, P_∞. The Reynolds number of the flow based on the free-stream velocity (U_∞) and hydrofoil chord length C_0 ($Re = U_\infty C_0/\nu$) ranged from 2.01×10^6 to 2.14×10^6, where ν is the liquid kinematic viscosity. Six pressure taps are installed on the top window to monitor static pressures for six locations upstream, within and downstream of the Venturi. An Omega PX203 pressure transducer was used to measure the absolute pressures at the taps. The free-stream air content was maintained below 20 % saturation at atmospheric pressure (oxygen concentration measured with Orion dissolved oxygen meter Model 810).

2.2. *Flow visualization*

Stereo particle imaging velocimetry (SPIV) was used to measure the vortical flow field at a location 1 cm upstream of the Venturi inlet and at 10 cm downstream of the Venturi inlet (figure 2). A double-pulsed light sheet 5 mm thick was created

perpendicular to the mean flow direction with two pulsed Nd:YAG lasers (Spectra Physics model Pro-250 Series), and three cylindrical lenses (60 mm, −150 mm and 200 mm focal length). Acrylic prisms were optically mounted to side windows of the test-section for viewing of the light sheet with reduced optical distortion. Double-pulsed images of the light sheet were acquired with two digital (LaVision FlowMaster 3S) cameras recording an image with 1280×1024 pixels. Two 50 mm Nikon lenses were used with Scheimpflug mounts to reduce optical distortion and aid in focusing on the light sheet. Optical distortion of the planar light-sheet images was corrected through a calibration procedure that employed the imaging of a regular grid (crosses separated by 4 mm) that was traversed in the streamwise flow. The grid was immersed in water during calibration. The flow was seeded with 15.3 μm average diameter silver coated glass spheres (Potters Industries). Velocity vectors were produced from the double-pulsed images using the LaVision image analysis software DaVis 6.0.4. Multi-pass processing with a final window size of 16×16 pixels was used with 50 % window overlap in the final pass to produce 159×97 in-plane velocity vectors at 0.56 mm spacing. The camera-imaging plane was not parallel to the light sheet, and it had an angular shift of 40° with the horizontal direction. The average vortical flow field was determined after processing and averaging 1000 individual vector fields. Oweis & Ceccio (2005) discussed the implication of vortex wandering on the averaged vortical flow field. The wandering of the single vortex in the present experiment was considered negligible. The uncertainty in the in-plane velocity measurements is estimated to be ±3 % whereas the out-of-plane component is estimated to be ±6 %.

2.3. *Single nucleus production*

Single cavitation bubbles were controllably produced in the core of the line vortex through the optical initiation of a small nucleus upstream of the Venturi (figure 1). Laser-induced bubbles were generated by optical breakdown near the axis of the vortex 10 mm before the inlet of the Venturi. A Q-switched Nd:YAG laser (Spectra Physics PRO 250) producing 10 ns light pulses with a maximum energy of 280 mJ at the 1064 nm wavelength was focused at the vortex centreline. The laser energy was reduced to the threshold necessary to create a single nucleus, and, by varying the free-stream pressure and laser energy, the initial size of the laser-induced nucleus could be approximately controlled (Tomita, Tsubota & Annaka 2003). The nucleus is a small bubble consisting of vapour and non-condensable gas that results from diffusion, plasma recombination, and chemical reactions. The free-stream dissolved gas content was kept below 20 % saturation, significantly decreasing the number of free-stream nuclei, and only rarely would a naturally occurring nucleus produce a vortex cavitation bubble.

2.4. *Acquisition of bubble images*

Images of the vortex cavitation bubbles were acquired with two 8-bit Phantom V9.0 high-speed movie cameras (figure 1). These cameras were set to an effective resolution of 1632×104 pixels at a frame rate of 8000 frames per second with a 15 μs exposure time. 50 mm Nikon lenses with 12 mm extension rings were used. Each camera has a 70 mm × 4.5 mm viewing area, and the fields of view were overlapped by 10 mm in the streamwise direction. A set of four 300 W incandescent lights was installed opposite the camera, and a light diffuser was used to prevent glare on the imager. A pulse delay generator (Stanford Research Systems model DG535) was used to trigger the camera with varying delays from the laser pulse that created the nucleus. These movie images were recorded digitally for post-processing.

2.5. *Acoustic measurements*

A high-bandwidth hydrophone (Brüel & Kjær Model 8103) was used to detect the cavitation noise created by the bubbles in the vortex. This hydrophone has an upper frequency limit of approximately 180 kHz. The hydrophone was mounted inside the small water reservoir, and placed on the top window of the test section, and the container was placed in a pool of water on top of the window to enhance the transmission of the acoustic pulses. This hydrophone was placed above the average location of bubble collapse, and the distance between the hydrophone and the bubble collapse is about 30 cm. Signals from the hydrophone were conditioned with a charge amplifier (Brüel & Kjær Model 2635), and digitally acquired using an oscilloscope sampling at 250 kHz with a record length of about 40 ms (TekTronix Model TDS430A).

3. Results – vortical flow field

3.1. *Analytical treatment of the vortical flow field*

The tip vortex created by the hydrofoil rolls up within one to two chord lengths downstream of the hydrofoil trailing edge. The velocity and pressure upstream of the Venturi are U_∞ and P_∞. The streamwise position is z, and the radial distance from the vortex axis is r. We will assume that the flow near the vortex is axisymmetric, although this will be revisited below. The flow in the plane orthogonal to the vortex axis can be approximated by a Gaussian vortex where radial velocity distribution of the vortex is given by:

$$u_\theta(r, z) = \frac{\Gamma_O(z)}{2\pi r}(1 - \exp(-\alpha(r/r_C(z))^2)). \tag{3.1}$$

Here, $\alpha = 1.255$ which makes r_C the 'core radius', defined as the radius where the tangential velocity is maximum. Both the core size and vortex strength, Γ_O, are potentially functions of z. The maximum tangential velocity is then given by

$$u_\theta(r_C, z) = \beta\frac{\Gamma_O}{2\pi r_C}, \tag{3.2}$$

where $\beta = 0.715$.

The pressure in the core of the Gaussian vortex is given by

$$\begin{aligned} P(r, z) - P(z) &= \int_\infty^0 -\frac{\rho u_\theta^2(r)}{r}\,\mathrm{d}r \\ &= -\rho\left(\frac{\Gamma_O}{2\pi r_C}\right)^2\left(\frac{1}{2(r/r_C)^2}\right)[-1 + 2\exp(-\alpha(r/r_C)^2) - \exp(-2\alpha(r/r_C)^2) \\ &\quad - 2\alpha(r/r_C)^2\,\mathrm{Ei}(\alpha(r/r_C)^2) + 2\alpha(r/r_C)^2\,\mathrm{Ei}(2\alpha(r/r_C)^2)] \end{aligned} \tag{3.3}$$

where $\mathrm{Ei}(x)$ is the exponential integral function, and $P(z)$ is the pressure at position z far from the vortex axis. The pressure at the vortex centreline is given by

$$\frac{P_C(z) - P(z)}{\rho} = -\eta\left(\frac{\Gamma_O}{2\pi r_C}\right)^2, \tag{3.4}$$

where $\eta = 0.870$.

The vortex may also have an axial velocity component that can also be described with a Gaussian profile, and it is expected that the axial velocity of the vortex core will change as the vortex passes through the Venturi. The streamwise velocity on the vortex axis is $U_C(z)$. If there is a non-uniform axial velocity at the centre of the vortex,

$U_C(z)$, the core pressure will be given by

$$\frac{P_C(z)-P_\infty}{\rho}=-\eta\left(\frac{\Gamma_O}{2\pi r_C}\right)^2+\frac{U_\infty^2}{2}\left[1-\left(\frac{U_C}{U_\infty}\right)^2\right]. \tag{3.5}$$

Darmofal *et al.* (2001) examined the flow of a Rankine vortex through an axisymmetric duct of varying cross-section, and used mass and energy conservation to derive a relationship between the Rankine vortex core area given the variation in the duct area and the inlet flow parameters:

$$\frac{\Omega_\infty^2}{a(z)/A_\infty}-\left(\frac{1}{a(z)/A_\infty}\right)^2+\left(\frac{U_\infty/U_{C,\infty}(1-a_\infty/A_\infty)}{A(z)/A_\infty-a(z)/A_\infty}\right)^2=\Omega_\infty^2-1+\left(\frac{U_\infty}{U_{C,\infty}}\right), \tag{3.6}$$

where $A(z)$ is the duct area, $a(z)$ is the vortex core area, and

$$\Omega_\infty=\frac{u_\theta(r_C,z)}{U_{C,\infty}}=\beta\frac{\Gamma_O}{2\pi r_C}\frac{1}{U_{C,\infty}} \tag{3.7}$$

is the Swirl number of the inlet vortex in the Gaussian vortex. Here, the subscript ∞ denotes the value at the inlet of the Venturi and the subscript C denotes the properties at the axis of the vortex, $r=0$. Darmofal *et al.* (2004) assume the streamwise velocity of the vortex core to be uniform. They also assume that the flow is inviscid and, consequently, that the vortex circulation is constant. We will use this relationship to estimate the local magnitude of the streamwise velocity in the vortex core as it passes through the Venturi to determine its influence on $P_C(z)$. We define the free-stream cavitation number as

$$\sigma_\infty=\frac{P_\infty-P_V}{\frac{1}{2}\rho U_\infty^2}. \tag{3.8}$$

The local cavitation number on the axis of the vortex is defined with the vortex properties upstream of the Venturi inlet, Γ_O and r_C:

$$\sigma_C(z)=\frac{P_C-P_V}{\frac{1}{2}\rho(\beta\Gamma_O/2\pi r_C)^2}, \tag{3.9}$$

where $\beta\Gamma_O/(2\pi r_C)$ is the maximum tangential velocity of the Gaussian vortex. The local cavitation number then is given by

$$\sigma_C(z)=-\frac{2\eta}{\beta^2}+\left(\frac{2\pi r_C U_\infty}{\beta\Gamma_O}\right)^2\left[1-\left(\frac{U_C}{U_\infty}\right)^2+\sigma_\infty\right]. \tag{3.10}$$

Inception in the core of the vortex can occur when $P_C<P_V$ or $\sigma_C<0$.

3.2. *Measurement of the vortical flow field*

Stereo PIV was used to measure vortical flow upstream of the Venturi inlet and in the throat of the Venturi in order to determine the strength, core size and axial velocity of the vortex upstream of the Venturi inlet and near the point of cavitation inception in the Venturi throat. Figure 3 shows the circumferentially averaged radial flow fields for the average vector fields with a fitted Gaussian radial velocity profile and a residual function, $\hat{u}_\theta(r)$, that is the difference between the fitted Gaussian profile and the experimental data (to be discussed in § 3.3). Figures 3(*a*) and 3(*b*) show the flow of the vortex for the case of the hydrofoil with the trip, and figures 3(*c*) and 3(*d*) show the flow for the hydrofoil with roughness, all with $U_\infty=10\,\mathrm{m\,s^{-1}}$. The tip vortex upstream of the Venturi inlet is nearly axially symmetric. These and similar flow fields

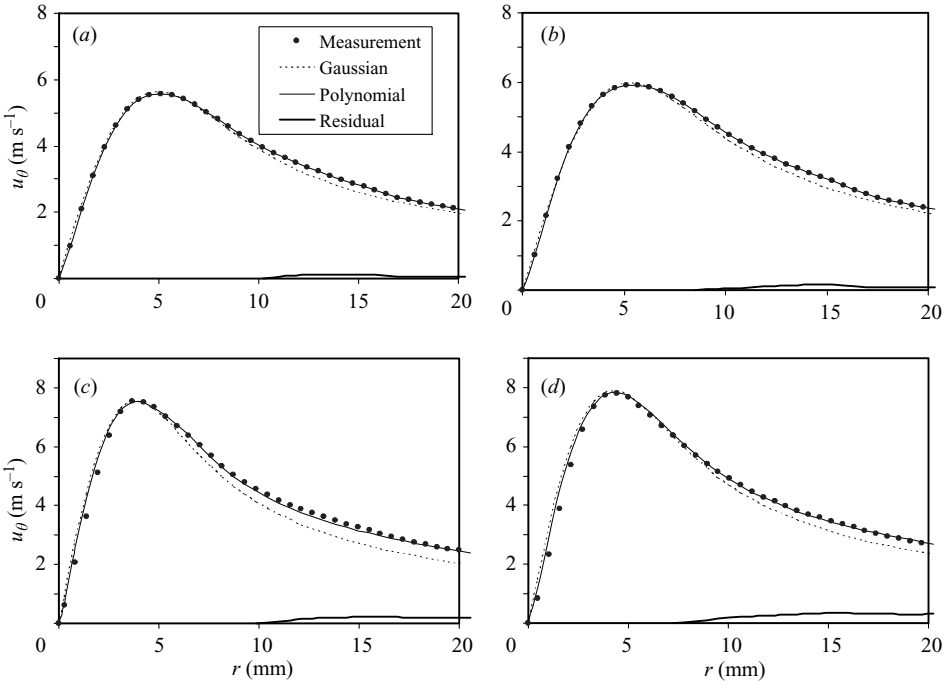

FIGURE 3. Average circumferential velocity, $u_\theta(r)$, derived from 1000 vector fields in the plane perpendicular to the line vortex. Conditions are defined in table 1. The measured circumferential velocity profile is fitted with a polynomial and compared with a fitted Gaussian velocity profile. The residual function shown is the difference between these two profiles. (*a*) T1, (*b*) T2, (*c*) R1, (*d*) R2.

	$\alpha = 4°$	(1)	$\alpha = 4.5°$	(2)
	Γ_O (m^2 s^{-1})	r_C (mm)	Γ_O (m^2 s^{-1})	r_C (mm)
Foil with trip (T)	0.252 ± 0.015	4.76 ± 0.31	0.288 ± 0.018	5.15 ± 0.35
Foil with roughness (R)	0.257 ± 0.013	3.75 ± 0.02	0.302 ± 0.015	4.20 ± 0.23

TABLE 1. Experimental conditions for the vortex properties in the Venturi with two different hydrofoil configurations. The vortex properties were identified from 1000 individual vector fields; $U_\infty = 10\,\mathrm{m\,s^{-1}}$. The four conditions are referred to as T1, T2, R1 and R2.

were used to determine the circulation and core size of the vortices under varying conditions. The properties of the fitted Gaussian profiles are presented in table 1. The circulation and core size from each individual flow field were determined, and these values were then averaged to determine the mean value and uncertainty stated in the table. The effect of vortex wandering was not significant, as the variation of the identified position of the vortex axis, $|\Delta\bar{x}|/r_C$, varied less than 6 % (see Oweis & Ceccio (2005) for a discussion of vortex identification and the effects of wandering). We will hereinafter refer to the four flow conditions as T1 and T2 for the foil with the trip, and R1 and R2 for the foil with roughness. A number of different free-stream pressures will be applied to vary the cavitation number along the vortex core for these four flow conditions. The streamwise (out-of-plane) velocity was nearly

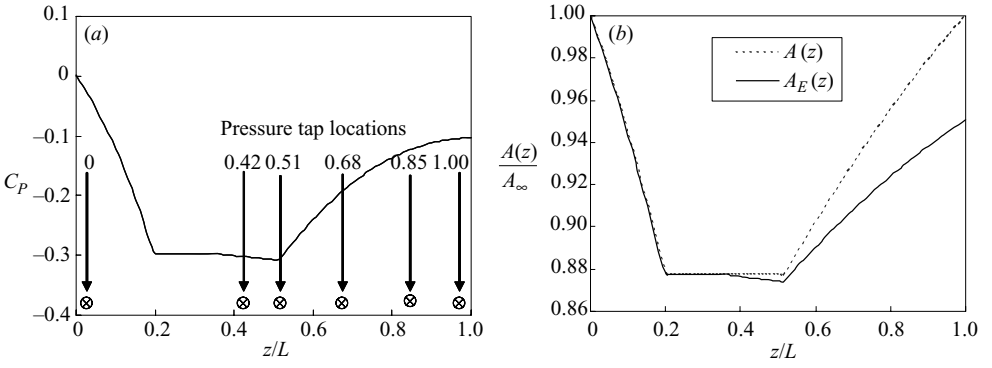

FIGURE 4. (*a*) The estimated pressure coefficient, $C_P = (P - P_\infty)/\frac{1}{2}\rho U_\infty^2$, in the Venturi as a function of position along the centre of the Venturi, z/L. (*b*) The normalized duct area, $A(z)/A_\infty$, as a function of distance. $A(z)$ is the actual duct area, and $A_E(z)$ is the effective duct area.

uniform, indicating that the vortex upstream of the Venturi inlet did not have an axial velocity deficit or surplus, within the uncertainty of the measurement.

SPIV measurements were also performed in the Venturi throat. Measurements in the throat did show some variation in circumferential velocity at a given radius owing to the asymmetry of the Venturi. The circulation of the vortex was conserved within experimental uncertainty. Also, these data indicated that the axial velocity of the liquid in the vortex core was approximately 3 % higher than the axial velocity of the fluid outside of the core. However, the limited resolution of the axial velocity component measured with the SPIV rendered this direct measurement of the axial velocity too uncertain to be used in the overall estimate of the core pressure. Therefore, we used the relationship of Darmofal *et al.* (2001) (equation (3.6)) to estimate the core velocity and pressure all along the vortex axis. The computed core velocities presented below were qualitatively consistent with the SPIV measurements in the Venturi core.

3.3. *Inferred pressure in the vortex core*

We will now estimate the pressure in the vortex core as it passes through the Venturi using both the measured flow-field data and the estimated core acceleration. The pressure will be modified by changes in the pressure away from the vortex core (i.e. pressure changes due to the bulk flow through the Venturi) and by additional acceleration of the streamwise flow in the vortex core. First, the influence of the Venturi area change and frictional losses on the pressure field experienced by the vortex were estimated. Figure 4(*a*) presents the estimated pressure coefficient,

$$C_P(z) = \frac{P(z) - P_\infty}{\frac{1}{2}\rho U_\infty^2}, \tag{3.11}$$

where $P(z)$ is the local pressure in the Venturi, away from the edge of the vortex core. The pressure coefficient is calculated using the measured pressures and the physical duct area, $A(z)$. The head loss coefficients for the three regions in the Venturi were matched with the measured pressures, and the pressure in the contraction of the Venturi is given by,

$$P(z/L) - P_\infty = C_C \tfrac{1}{2}\rho(U_\infty^2 - U^2(z/L)) \qquad (0 < z/L < 0.2). \tag{3.12}$$

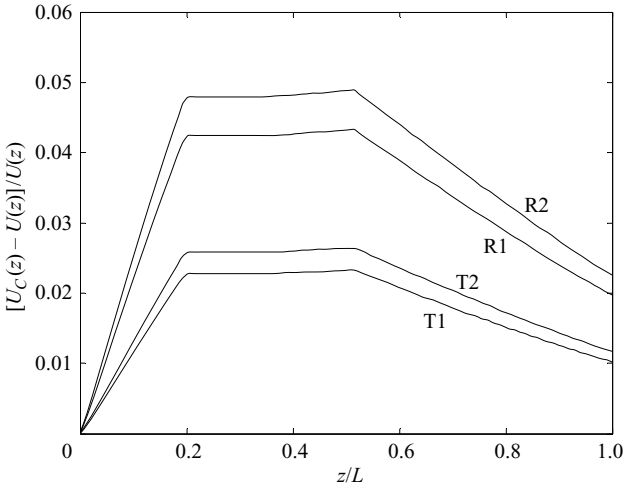

FIGURE 5. The computed average axial velocity of the vortex core as a function of axial distance through the Venturi. $U(z)$ is the average velocity in the Venturi, and $U_C(z)$ is the average core velocity. Conditions are given in table 1.

The pressure in the throat with head loss due to friction is given by,

$$P(z/L) - P(0.2) = C_S \tfrac{1}{2}\rho U^2(z/L) \qquad (0.2 \leqslant z/L < 0.5). \tag{3.13}$$

Also, the pressure in the diffuser is given by,

$$P(z/L) - P(0.5) = C_S \tfrac{1}{2}\rho(U^2(0.5) - U^2(z/L)) \qquad (0.5 < z/L < 1). \tag{3.14}$$

The head loss coefficients were determined from the measured wall pressures along the Venturi: $C_C = 1.01$, $C_S = 0.005$ and $C_D = 0.675$. Lastly, these data were used to compute the effective cross-sectional area of the Venturi, $A_E(z)$, for use in evaluating equation (3.6). The physical Venturi cross-sectional area and the effective cross-sectional area are shown in figure 4(*b*).

The average vortex core velocity was calculated from the vortex core area, $a(z)$, which results from the solution of equation (3.6). Figure 5 presents the average streamwise flow velocity through the Venturi, $U(z)$, and the estimated vortex core velocities, $U_C(z)$, for the four conditions in table 1. The extent of the calculated streamwise core velocities, $[U_C(z) - U(z)]/U(z)$, varies from 1.5 % to 5 %. These modest increases are within the uncertainty of the SPIV measurement, but are consistent with the observed positive acceleration of the vortex core flow in the Venturi throat.

While seemingly small, these changes in the core radius will lead to appreciable changes in the vortex core pressure. Equation (3.5) was then used to compute the pressure coefficient along the vortex axis:

$$C_{P,C}(z) = \frac{P_C(z) - P_\infty}{\frac{1}{2}\rho(\beta\Gamma_O/2\pi r_C)^2} = -\frac{2\eta}{\beta^2} + \left(\frac{2\pi r_C U_\infty}{\beta\Gamma_O}\right)^2 \left[1 - \left(\frac{U_C}{U_\infty}\right)^2\right]. \tag{3.15}$$

The results are shown in figure 6. The second term on the right-hand side accounts for the local increase of the axial velocity inside the vortex core. If there were no local increase of the axial velocity inside vortex core, then $U_C(z) = U(z)$ and the change in pressure coefficient would be due solely to the average pressure change of the flow in the Venturi. The lowest pressure occurs in the core of the vortex at the exit of the Venturi contraction.

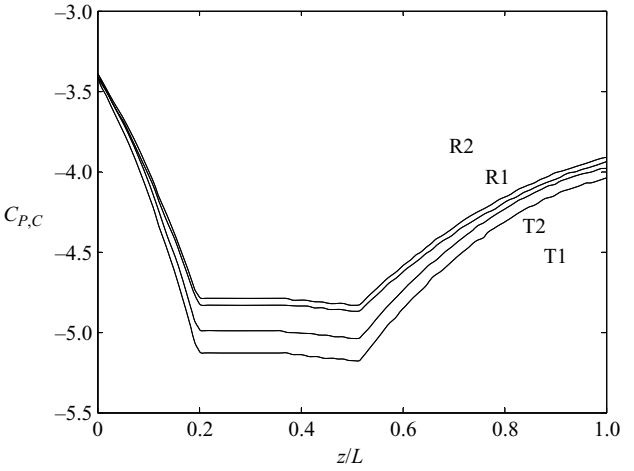

FIGURE 6. The estimated pressure coefficient at the vortex axis as a function of axial distance through the Venturi. Conditions are shown in table 1; $C_{P,C} = (P_C(z) - P_\infty)/(\rho(\beta\Gamma_O/(2\pi r_C)^2/2)$.

It is worth noting that the inlet velocity profiles are similar to but not identical to the Gaussian velocity distribution (figure 3). The rate at which the radial velocity decays is slower than the rate predicted by the Gaussian model. However, this effect has only a small influence on the core pressure. The radial velocity data in figure 3 can be represented by the sum of a Gaussian vortex (equation (3.1)) and a residual function, $\hat{u}_\theta(r)$, as illustrated in figure 3. The contribution of $\hat{u}_\theta(r)$ to the computed core pressure can be determined by integrating the Euler equation as in (3.3). For the vortices studied here, the change in the estimated core pressure coefficient, $C_{P,C}(z)$, is less than $\pm 1\,\%$, and thus the influence of the non-Gaussian tangential velocity components is negligible.

4. Results

4.1. *Examples of individual vortex cavitation bubbles*

The cavitation bubbles in the core region of the vortex develop according to the following steps. First, the nucleus created by the laser pulse convects into a region where the flow is in tension (i.e. negative pressure). If the tension is sufficiently strong, the nucleus will grow explosively. The critical radius along the vortex axis of a small clean gas bubble, $R_C(z)$, is approximately given by

$$\frac{4S}{3R_C(z)} < P_V - P_C(z), \tag{4.1}$$

where S is the surface tension (Brennen 1995). The nuclei created by the laser typically cavitate when the pressure in the core is between $-2\,\mathrm{kPa} < P_C(z) < 0\,\mathrm{kPa}$ suggesting that the critical radii of the nuclei are of the order of 10 to 100 μm. The pressure profile along the vortex axis does not change for fixed flow conditions. However, the size of the cavitating nucleus does vary. This leads to variation in the nuclei's critical pressure and therefore the location of inception. Arndt & Maines (2000) discuss this effect in the context of 'weak' and 'strong' water after observing the location of tip-vortex inception downstream of a series of elliptic hydrofoils. In the experiment by Arndt & Maines (2000), a tip vortex was rolling up downstream of the hydrofoil,

and the position of minimum core pressure existed at a fraction of a chord length downstream. In weak water, there were relatively large nuclei that cavitated when the core pressure just reached vapour pressure near the point of vortex formation at the tip of the hydrofoil. Stronger water had fewer, smaller nuclei, and a significant tension must be present before they incept. In these cases, inception took place farther downstream of the foil tip where the vortex had completed rolling up. Similar nuclei size effects were manifest in the present study. Because the laser light pulse produced a range of nuclei sizes, the position of inception occurred over a range of axial locations and hence tensions.

The bubble will usually retain its cylindrically elongated shape until it convects into the region of pressure recovery. Figure 7 presents examples of the growth and collapse of cavitation bubbles for each of the four vortex conditions of table 1. A time series of bubble images is shown, and these images are used to determine the radius of a circle that encloses the cross-section of the elongated bubble, where the cross-section is perpendicular to the axis of the elongated bubble and length history of the bubbles. The volume is also computed after measuring the local bubble radii and employing the assumption of bubble axisymmetry. Also presented is the accompanying hydrophone signal created by the bubble during inception, splitting and collapse. The cavitation numbers of the flows were selected such that bubble growth and collapse would largely take place in the camera field of view. The bubbles formed in the vortices share some general features. The growing nucleus begins as a nearly spherical bubble. It then becomes ellipsoidal and ultimately elongated as the extent of the bubble growth in the radial direction is arrested by the increase in pressure away from the vortex axis. The bubble continues to grow along the axes of the vortex while the pressure on the vortex axis remains below vapour pressure, and depending on the duration that the bubble is in tension, the length of the bubble can grow to many times its diameter.

During this period of elongation, disturbances can exist on the bubble interface as it slowly revolves about the bubble axis, and these surface waves can lead to volume oscillations of the bubble and the local fission of the bubble. Then, as the pressure rises, the bubble begins to collapse. The rate at which the bubble surface collapses can vary in the radial and axial directions. Under some conditions, the collapsing bubble may fission to form smaller, nearly spherical sub-bubbles at its ends. Or, the bubbles may split into multiple bubbles when the core pressure changes from tension to positive pressure. Pulses of noise are often, but not always, associated with bubble growth, fission and collapse. The bubble shape and size is a function of both the vortex properties and the free-stream cavitation number. The location where the vortex core pressure falls below vapour pressure will vary with the vortex properties and the cavitation number. But, for the cases examined here, the region of tension begins near the end of the Venturi throat. In some cases, images of the bubble collapse were captured by the high-speed imaging, whereas in others, the bubbles collapsed outside the cameras' field of view.

4.2. *Average bubble radius and length*

Figures 8 and 9 present the average length and radius of the observed bubbles for varying cavitation number and vortex properties. A hundred individual images for each case were averaged. The magnitude and extent of tension (e.g. negative fluid pressure) that the bubbles experience will vary with the cavitation number. For most of the cases, the bubbles begin to grow in the range $0.4 < z/L < 0.5$. The growth of the bubbles in the radial direction is rapid. Initial bubble radial growth and final collapse occur over a very short time interval that is usually shorter than the framing

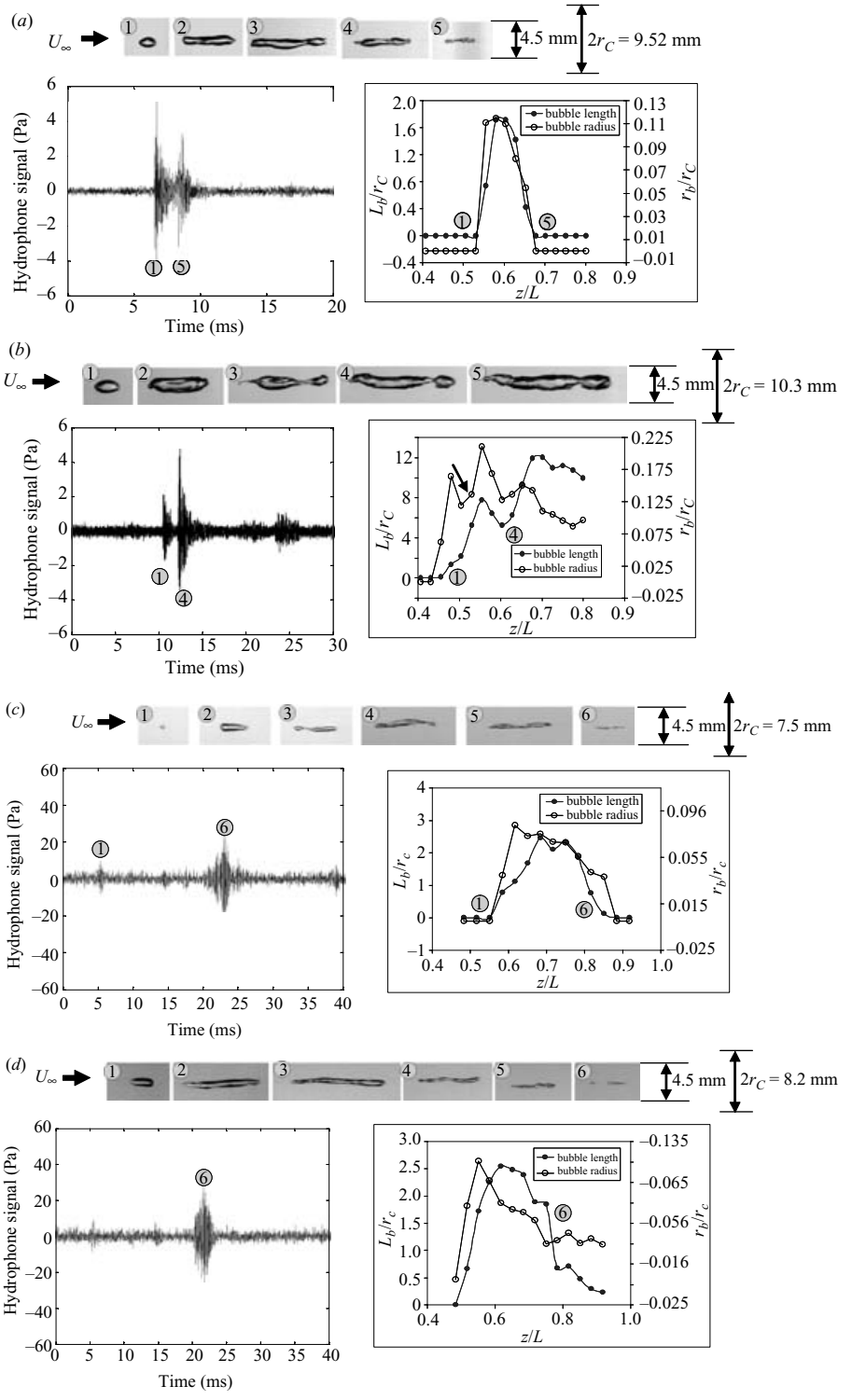

FIGURE 7. Images of individual cavitation bubbles taken from a video record to illustrate the bubble shape history and have varying time intervals. The video record was used to compute the length and average radius of the bubble as a function of position within the Venturi. Also shown are the corresponding acoustic signal detected from the hydrophone; (*a*) T1, $\sigma_\infty = 1.74$, (*b*) T2, $\sigma_\infty = 1.74$, (*c*) R1, $\sigma_\infty = 2.75$, (*d*) R2, $\sigma_\infty = 2.95$.

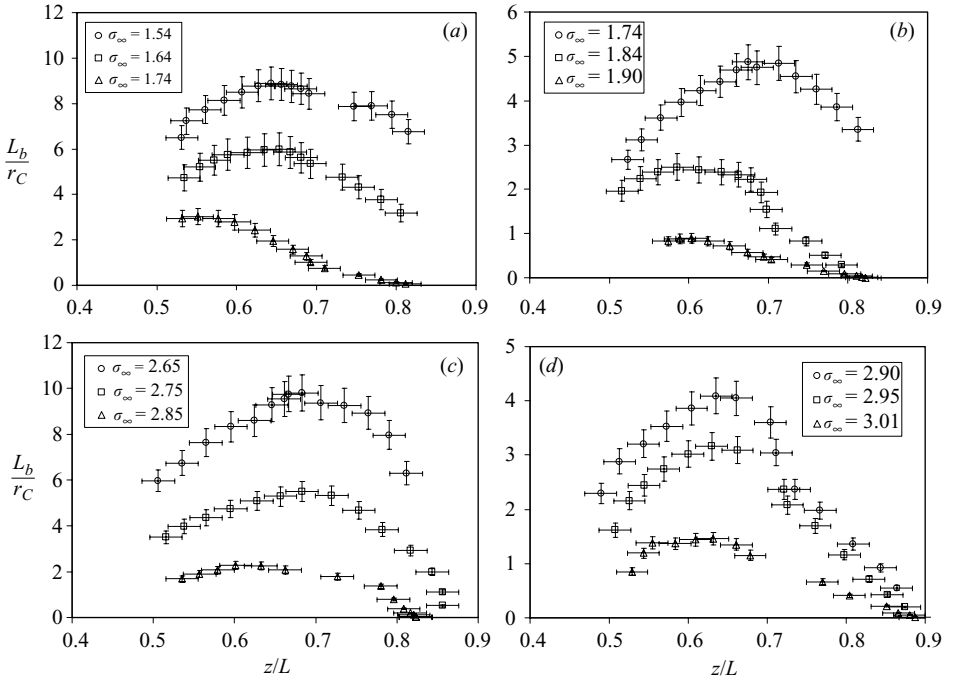

FIGURE 8. The average bubble length normalized by the vortex core radius as a function of distance along the Venturi for varying free-stream cavitation numbers; bubble length (solid symbols) and bubble radius (open symbols). Conditions are given in table 1. (*a*) T1, (*b*) T2, (*c*) R1, (*d*) R2.

rate of the camera. Therefore, the data in the figure 9 correspond to measurements after the bubble has undergone its rapid initial growth. This is seen in figure 9, where the maximum extent of the cylindrical bubble's radius usually occurs near $z/L = 0.5$, the position of highest tension is at the exit of the Venturi throat, and the magnitude of the radius begins to decrease as the bubbles convect into the pressure recovery region. Examination of the bubble length shows that the bubble continues to grow along the axial direction even as the pressure is increasing. The axial growth of the bubble is arrested around $z/L = 0.7$, and then the bubble begins to contract.

The data from figure 6 were used to determine $\sigma_C(z)$, and the average bubble characteristics were plotted as a function of the local core cavitation number. The difference in $\sigma_C(z)$ based on the different choice of axial locations is small compared to the propagated uncertainty in $\sigma_C(z)$ owing to the variability in the vortex properties and estimated core axial velocity and the free-stream measurements. The total uncertainty of $\sigma_C(z)$ was estimated to be $\pm 15\,\%$. This is calculated from the uncertainty of tangential velocity measurement and the measurement of the wall mean pressures.

Figure 10 presents the bubble radius as a function of $\sigma_C(z)$. Note that the bubble radius is finite even when $\sigma_C(z) > 0$. This occurs because a finite time is required for the bubble to collapse after the bubble convects into a region of higher pressure. When the elongated bubbles convect in a region of high tension, the radius of the bubble does not change very much, the ratio of r_b/r_C falls in the range $0.05 < r_b/r_C < 0.15$. The observation that the bubbles are a small fraction of the viscous core radius was also observed by Arndt & Maines (2000).

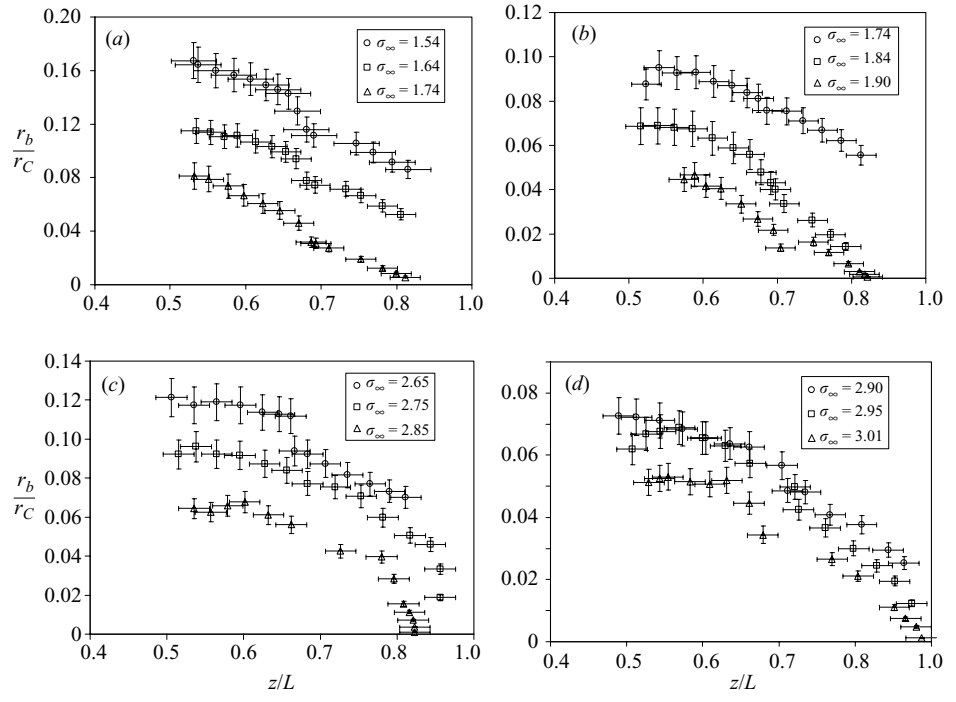

FIGURE 9. The average bubble radius normalized by the vortex core radius as a function of distance along the Venturi for varying free-stream cavitation numbers; bubble length (solid symbols) and bubble radius (open symbols). Conditions are given in table 1. (*a*) T1, (*b*) T2, (*c*) R1, (*d*) R2.

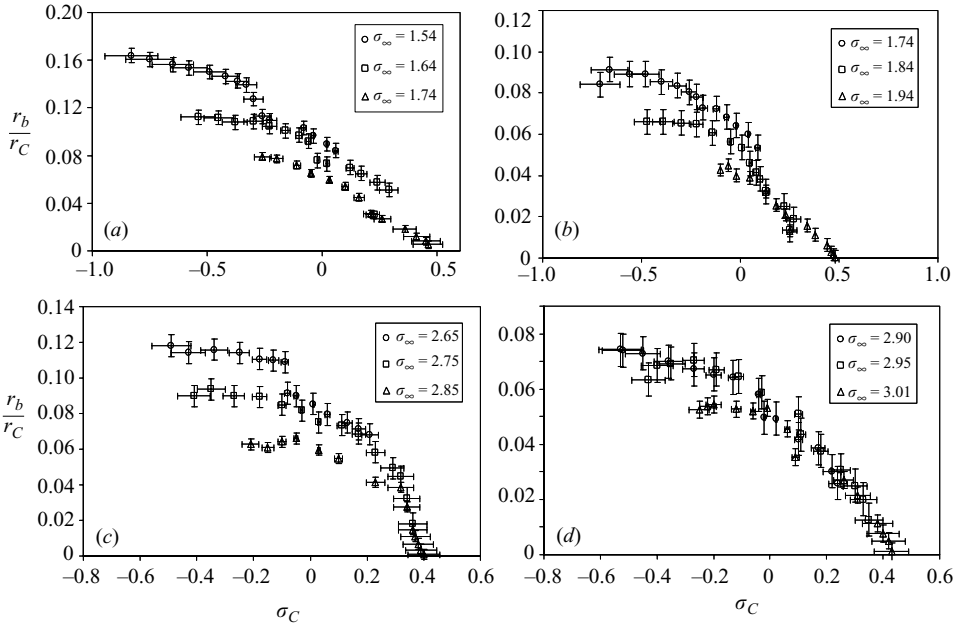

FIGURE 10. The average bubble radius as a function of the cavitation number at the vortex axis for varying free-stream cavitation numbers. Conditions are given in table 1. (*a*) T1, (*b*) T2, (*c*) R1, (*d*) R2.

The diameter of a cylindrical bubble in a two-dimensional vortex has been predicted analytically for a Rankine vortex by Arndt & Keller (1992). They employed conservation of angular momentum to show that the radius of the vapour bubble would be $r_b/r_C = 1/\sqrt{2}$ or 71 % of the initial core radius. However, it was acknowledged that the observed bubbles were significantly smaller in radius, as in the present study. Following this analysis for a Rankine vortex, we can examine the placement of a vapour cylinder in the core of a Gaussian vortex. The non-cavitating Gaussian vortex is defined with Γ_O and r_C. The liquid flow field of the cavitating vortex, however, can take on any profile and need not be Gaussian. We can define a Gaussian like profile in this case,

$$u_{\theta,b}(r, z) = \frac{\Gamma_{O,b}(z)}{2\pi(r - \gamma r_b)}(1 - \exp(-\alpha[(r - \gamma r_b)/(r_{C_b} - \gamma r_b)]^2)), \tag{4.2}$$

where $\Gamma_{O,b}$, r_{Cb} and γ are parameters of the cavitating vortex. The parameter γ can vary in the range $0 < \gamma < 1$. When $\gamma = 0$, the liquid velocity profile is the same as that of a single-phase vortex, where the maximum tangential velocity will occur at $r = r_C$, and vapour occupies the region $0 < r < r_b$. The tangential velocity at the bubble interface would be finite with the value

$$u_{\theta,b}(r_b) = \frac{\Gamma_{O,b}}{2\pi r_b(1 - \gamma)}(1 - \exp(-\alpha[(r_b(1 - \gamma)/(r_{Cb} - \gamma r_b)])^2)). \tag{4.3}$$

Conversely, if $\gamma = 1$, the tangential velocity at the bubble interface is zero. Lastly, the bubble contents are at vapour pressure, prescribing a boundary condition on the bubble surface.

We wish to determine the elongated bubble radius, r_b, as a function of the three non-cavitating vortex flow parameters: Γ_O, r_C and σ_C. The cavitating vortical flow is described by three parameters: $\Gamma_{O,b}$, r_{Cb} and γ. Therefore, four relationships are required to close the problem.

Conservation of angular momentum, Σ, provides one relationship:

$$\Sigma = \rho \int_0^\infty 2\pi r^2 u_\theta \, \mathrm{d}r. \tag{4.4}$$

We will assume that the growth of the bubble does not lead to torque on the liquid.

Secondly, we will consider the conservation of kinetic energy:

$$KE = \rho \int_0^{r \gg r_C} 2\pi r u_\theta^2 \, \mathrm{d}r. \tag{4.5}$$

The integral of the kinetic energy is not bounded as the limit of integration becomes large. Therefore, we will select a finite upper limit of integration of $10r_c$. Further increases of this limit are found not to change the solution. Note that the kinetic energy is not strictly conserved. The kinetic energy of the bulk fluid will be changed as the growing bubble works against the fluid. We will assume that the boundary work is negligible, since the work done by the expanding bubble is one to two orders of magnitude smaller than the total kinetic energy. We make this estimate assuming that the bubble is expanding against a constant pressure equal to vapour pressure. The actual work that the bubble performs on the fluid, however, depends on the volume–pressure history of the growing bubble. Nevertheless, the assumption that there is no loss or gain of kinetic energy in the liquid owing to the growing bubble is reasonable.

Thirdly, the pressure at the bubble boundary under equilibrium conditions is vapour pressure, and this provides the last condition. The Euler equation can be integrated

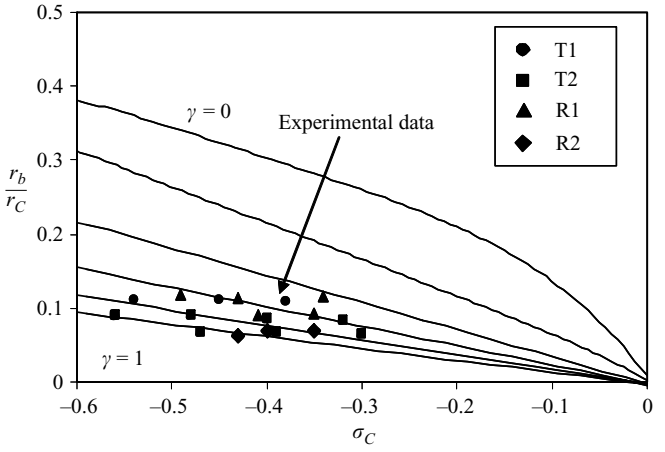

FIGURE 11. The calculated bubble radius in the core of a two-dimensional Gaussian vortex for varying parameter, $\gamma = 0$, 0.2, 0.4, 0.6, 0.8 and 1.0. The experimental data from the present experiment are also plotted. Conditions are given in table 1.

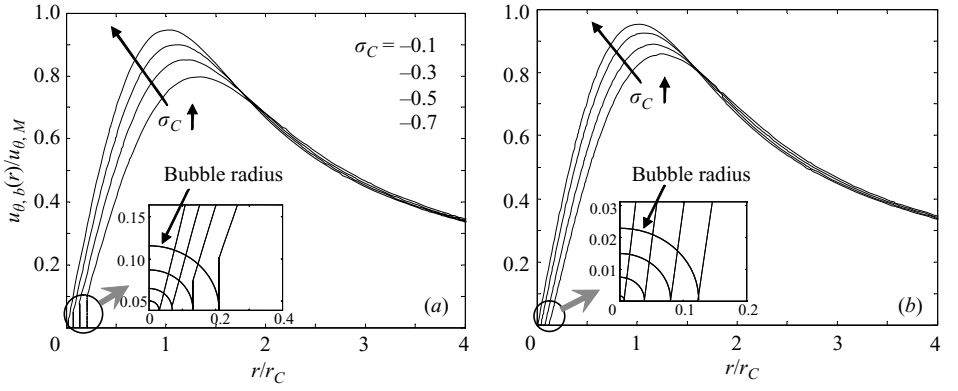

FIGURE 12. The calculated tangential velocity profile of a two-dimensional Gaussian vortex with a bubble at the axis. The tangential velocity is normalized by maximum tangential velocity of the flow without the bubble present, and radial dimension is normalized by the non-cavitating vortex core radius. Calculations (*a*) for $\gamma = 0.6$ and (*b*) $\gamma = 1$ are shown.

to relate the pressure at the bubble interface to the pressure far from the vortex, as in (3.3). A fourth conservation relationship was not employed. Instead, γ is considered to be a free parameter.

Figure 11 presents the resulting bubble radius as a function of cavitation number for a range of γ. Also plotted are the experimental data from figure 10 corresponding to the observations where the bubbles are in a region of tension and the radius has ceased to vary. The data suggest a value of $0.6 < \gamma < 1$. Figure 12 shows tangential velocity profiles for the cases of $\gamma = 0.6$ and 1. In both cases, the tangential velocity of the bubble interface is small, reaching about 10 % of the maximum tangential velocity of the non-cavitating vortex. In the present experiments, this would be around $0.3\,\mathrm{m\,s^{-1}}$ for the average cavitation numbers examined, and this is similar to the observed rotation rates of between 0.2 and $0.4\,\mathrm{m\,s^{-1}}$ obtained from examination of the bubble movies. The variation in the equilibrium r_b/r_C for the different vortex properties

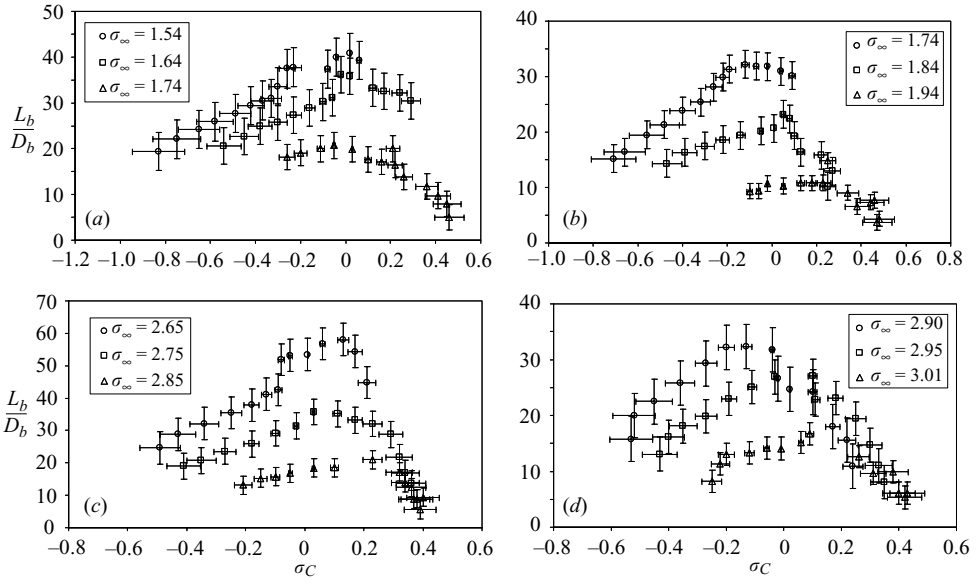

FIGURE 13. The average bubble aspect ratio as a function of the cavitation number at the vortex axis for varying free-stream cavitation numbers. Conditions are given in table 1. (*a*) T1, (*b*) T2, (*c*) R1, (*d*) R2.

suggests that the value of the tangential velocity at the bubble surface (related to γ in the model) may not be uniquely determined for any single vortex, but is the product of the detailed history of the bubble growth. In this case, r_b/r_C is not simply related to the ratio $\Gamma_O/2\pi r_C$ that scales the radial pressure field of the non-cavitating flow. We also examined laser-induced single vortex cavitation bubbles without the Venturi. Inception occurred immediately downstream of the laser pulse location, and the bubble grew in the axial direction to fill the vortex core. The equilibrium bubble radii of these elongated bubbles also ranged between 0.08 and 0.18 with σ_C from -0.1 to -0.25. These results are similar to the radii measurements for the bubbles passing through the Venturi. Hence, the axial pressure gradient present in the Venturi flow had little effect on the equilibrium bubble radius.

Figure 13 presents the average bubble aspect ratio as a function of $\sigma_C(z)$. These data show that the bubbles quickly become elongated once inception has taken place. As is the case for r_b/r_C, the bubble aspect ratios are not simply related to the vortex properties and the cavitation number history (i.e. the data are not collapsed by these quantities alone). Bubbles with aspect ratios of over 50 were observed. Figure 14 presents the normalized bubble volume computed with the assumption of axisymmetry. The volume of the elongated bubbles are compared to a spherical bubble with a radius equal to the vortex core radius. The maximum normalized volumes vary widely from 0.02 to 0.3 times the volume of a sphere with radius equal to the core radius.

4.3. *Dynamics and splitting of the bubbles*

The rate of bubble growth and collapse was also examined. Because of the limited frame rate of the imaging system, we were limited to measuring the slower bubble motions that occur immediately after inception. At inception, the expansion of the nucleus is very rapid, especially if the nucleus was small and incepted in a region of high tension. Expansion of the near-spherical bubble to its largest radial extent would

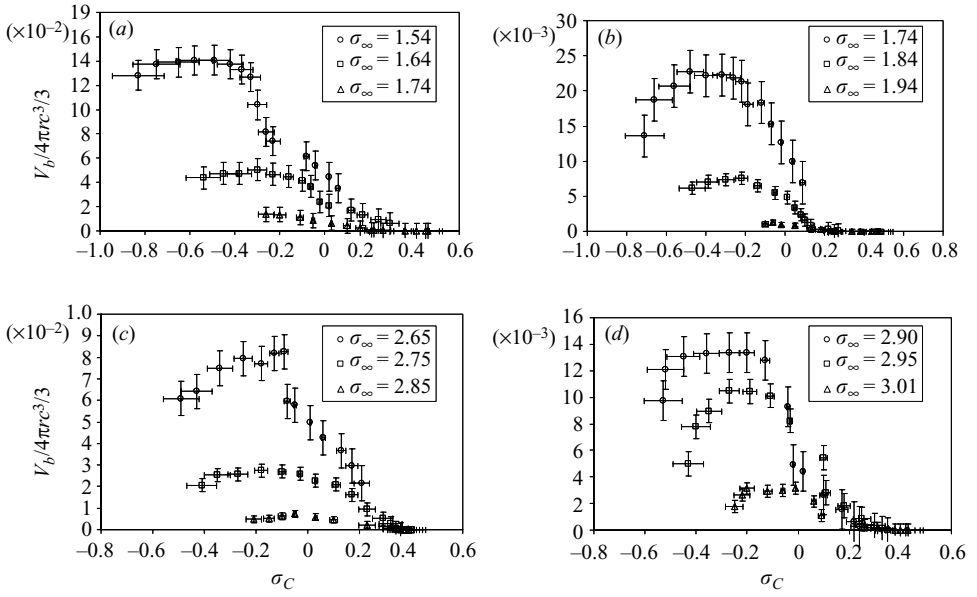

FIGURE 14. The average bubble volume as a function of the cavitation number at the vortex axis for varying free-stream cavitation numbers. Conditions are given in table 1. (*a*) T1, (*b*) T2, (*c*) R1, (*d*) R2.

take place in less than one frame of the movie image spanning 125 μs. This would make the average incipient radial velocities of the order of $10\,\mathrm{m\,s^{-1}}$, although the bubble wall velocity and acceleration at the moment of explosive growth are much higher. This is illustrated in figure 7, where the explosive growth of the smaller nuclei (occurring farther downstream in the throat) would produce explosive growth and an accompanying acoustic pulse. The growth of larger nuclei would be slower since they grow with lower tension, and the acoustic pulse they created had lower magnitude.

Figure 15 presents the axial bubble velocities as a function of the local cavitation number. The axial growth rate ($\dot{L} > 0$) also increases at lower cavitation number with higher tension. The trends of decreasing axial collapse rate with increasing cavitation number results from the dynamics of the bubble in the pressure recovery region of the Venturi. Here, the highest cavitation numbers occur when the bubble is near its minimum volume immediately before the final collapse.

Arndt & Maines (2000) analysed the process of axial bubble growth in order to scale the growth rate with the driving pressure. They derived an equivalent expression of the Rayleigh–Plesset equation for bubble growth in the axial direction assuming a value of the apparent mass of the axially growing bubble that was proportional to the displaced volume of the bubble. They concluded that the rate of axial bubble growth scales with the differential driving pressure,

$$\dot{L}_b \sim \kappa \sqrt{\frac{2(P_C - P_V)}{\rho}} = \kappa \left(\frac{\beta \Gamma_O}{2\pi r_C} \right) \sqrt{\sigma_C}. \tag{4.6}$$

Arndt & Maines (2000) showed that $\kappa = 2/\sqrt{c_m}$ for the near-spherical bubbles, where c_m is the added mass coefficient scaling the displaced bubble volume. A value of $\kappa \approx 2.1$ was determined from experimentally observed bubble growth for the near-spherical bubbles. Near the point of inception, the radial growth rate of the bubbles

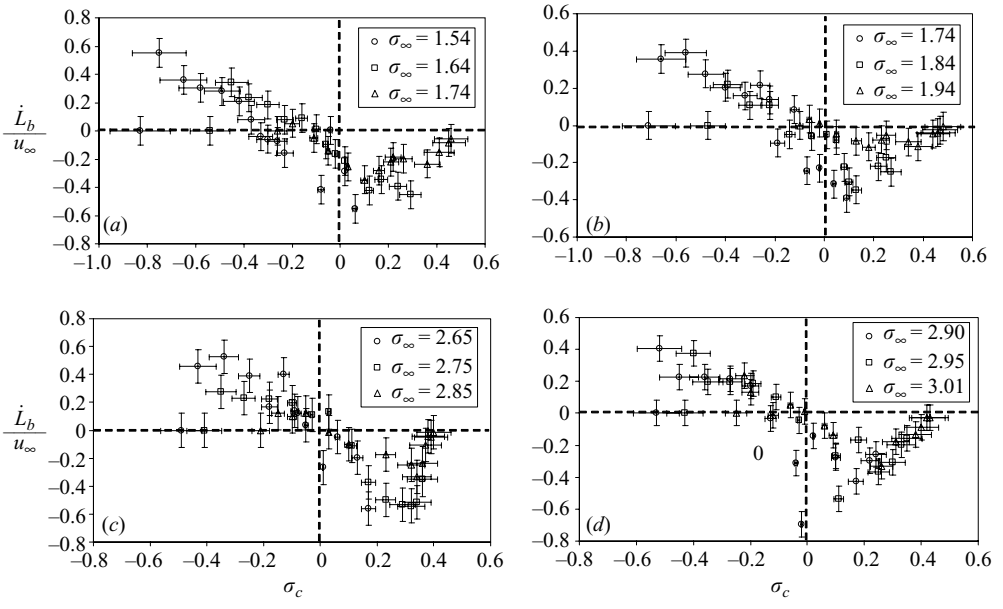

FIGURE 15. The growth and collapse rate of the bubbles in the axial direction as a function of the cavitation number at the vortex axis for varying free-stream cavitation numbers. Conditions are given in table 1. (*a*) T1, (*b*) T2, (*c*) R1, (*d*) R2.

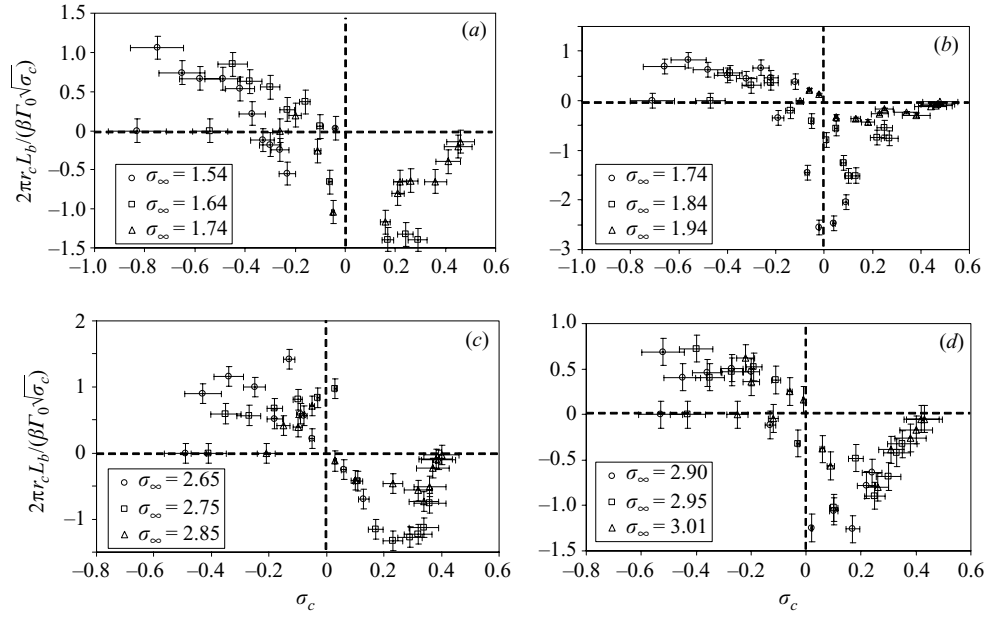

FIGURE 16. The scaled rate of axial growth and collapse as a function of the cavitation number at the vortex axis for varying free-stream cavitation numbers. Conditions are given in table 1. (*a*) T1, (*b*) T2, (*c*) R1, (*d*) R2.

is the largest and of the order of $10\,\mathrm{m\,s^{-1}}$. This is consistent with a value of κ of two or greater. Figure 16 presents the normalized axial growth rate. The bubbles that are highly elongated with a nearly unchanging radius indicate that $\kappa \approx 1$ for the bubble

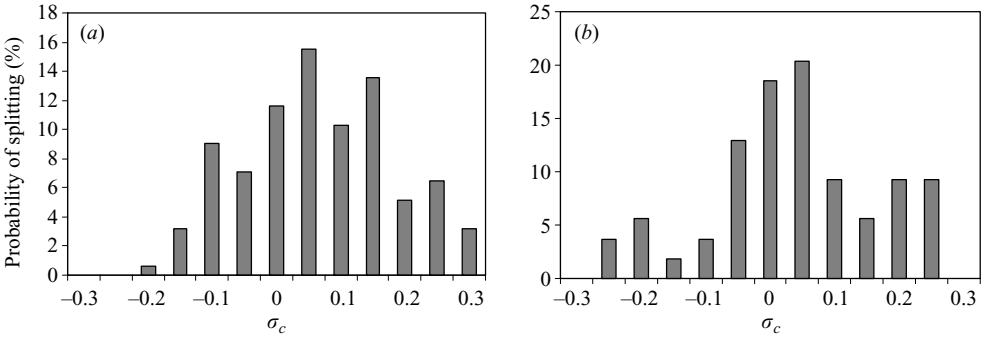

FIGURE 17. The probability of bubble splitting as a function of the cavitation number at the vortex core. (*a*) T2, (*b*) R1.

growth rate in the axial direction. These data suggest that the added mass coefficient for the axially expanding bubble is probably not a constant, but varies with the aspect ratio of the bubble.

As the bubbles grow and collapse, perturbations on the gas–liquid interface form. These surface disturbances can lead to fission of the elongated bubbles. Moreover, during collapse of the bubble, the difference between the radial and axial collapsing rates can lead to the pinch-off of sub-bubbles at the extreme end of the bubble, as shown numerically by Choi & Chahine (2004). Examples of such splitting events can be seen in figure 7. Figure 17 shows the probability that a bubble will split based on the local cavitation number. Bubbles were observed to split, even when they were largely in regions of tension, and this is due to the presence of disturbances on the bubble interface. However, the highest likelihood of splitting occurs when the pressure surrounding the bubble is larger than vapour pressure, and the bubble has initiated the process of collapse.

4.4. *Noise produced by bubble growth, splitting and collapse*

The noise produced by individual cavitation bubbles was recorded to determine which bubble processes led to the production of measurable noise. A discussion of the noise produced by slightly deformed bubbles in a vortex and the challenges of measuring such noise is presented in Oweis *et al.* (2004). A brief summary will be provided here. The sharp pressure pulse created by a collapsing cavitation bubble may be approximated as $P_a(r,t) = P_S \mathrm{e}^{-t/\theta}$, and the pulse widths can be very short for highly focused collapse. Pulse widths measured with optical and piezoelectric transducers are of the order of 10 to 100 ns (Vogel & Lauterborn 1988). The peak amplitude of the response will be proportional to P_S, and the initial pulse width will be proportional to $1/\varpi_n$, the natural frequency of the hydrophone, if $1/\varpi_n \gg \theta$. The measured pulse widths were typically $10 \pm 2\,\mu\mathrm{s} \approx 1/\varpi_n$, which is consistent with the reported hydrophone natural frequency used in the present study. The actual acoustic impulse will be approximately $I(r_H) \approx P_S(r_H)\theta(r_H)$ at the location of the hydrophone, r_H. The measured acoustic impulse, I_m, will scale as

$$I_m(r_H) \approx \frac{P_S(r_H)}{\varpi_n}\theta(r_H)\varpi_n \approx P_S(r_H)\theta(r_H), \tag{4.7}$$

based on the dynamic impulse response function of the hydrophone. However, the measured peak pressure and the pulse duration will be approximated by $P_S(r_H)$ $\theta(r_H)\varpi_n$ and $1/\varpi_n$, respectively. The maximum bubble volume accelerations achieved

and the resulting amplitude and time scale of the emitted pressure wave is affected by the amount of non-condensable gas in the cavity, the collapsing pressure (ΔP), and the topology of the collapsing bubble.

The maximum mechanical potential energy of the bubble may be used to scale the acoustic impulse produced by the collapsing bubble, E_M,

$$E_M = \tfrac{4}{3}\pi r_{b,M}^3 \Delta P. \tag{4.8}$$

The energy radiated from the bubble after the collapse and rebound, E_R, is given by

$$E_R(r) = \eta_R \frac{4\pi r^2}{\rho c} \int_0^\infty P_a^2 \, \mathrm{d}t, \tag{4.9}$$

where η_R is the proportion of mechanical potential energy that is converted into acoustic energy. Vogel & Lauterborn (1988) have shown that up to 90 % of a bubble's mechanical energy can be converted to acoustic energy during the first collapse of spherical laser-produced cavitation bubbles, but the percentage can be reduced substantially if the collapsing bubble is non-spherical. The measured peak shock pressure, P_S, is expected to scale with the maximum potential energy:

$$P_S \sim \frac{1}{2r_H}\left(\frac{\rho c E_R}{\pi\theta}\right)^{1/2} \sim \frac{1}{2r_H}\left(\frac{\eta_R \rho c E_M}{\pi\theta}\right)^{1/2}. \tag{4.10}$$

The acoustic impulse would then scale as

$$I_m(r_H) \sim \frac{1}{2r_H}\left(\frac{\eta_R \rho c E_M \theta}{\pi}\right)^{1/2} \sim \frac{1}{r_H}\left(\tfrac{1}{3}\eta_R \rho c \Delta P R_M^3 \theta\right)^{1/2}. \tag{4.11}$$

The functional relationship between θ and the other parameters of the flow are not straightforward, especially in the case of non-spherical bubble splitting and collapse.

In the present study, the bubbles were sometimes observed to produce noise during growth, splitting and collapse. The scaling analysis presented above is applicable to the collapse of near spherical bubbles. However, we will use this scaling to compare the relative magnitude of the measured growth and splitting noise with that of collapsing bubbles. In the case of the elongated bubbles, we will scale the bubble volume with the maximum radial dimension of the bubble, $r_{b,M}$, rather than the radius of a sphere with the equivalent maximum bubble volume. Sub-bubbles that split from the ends of the elongated bubbles will have dimensions closer to the axial diameter of the parent bubble. Hence, $r_{b,M}$ is a better scale to determine the maximum volume of the collapsing sub-bubble. We will assume that $\eta_R = 1$ and $\theta = 10$ ns for all the cases examined in order to make a comparison of the impulse produced from growth, splitting and collapse. The pressure difference ΔP is derived from the local cavitation number, σ_C.

Figure 18 presents the scaled acoustic impulse $\hat{I} = I_m r_H / (\frac{1}{3}\eta_R \rho c \Delta P r_{b,M}^3 \theta)^{1/2}$ for noise produced by growing and splitting bubbles for cases T1 and T2 and for the collapse noise for cases R1 and R2. Growth noise was detected when a small nucleus convected into a region of higher tension before incepting, leading to a higher rate of volume acceleration during growth. Detectable noise from splitting was rare, and it was on the order of the noise produced by bubble growth. The impulse produced by collapsing bubbles was about 10^3 times that of the growth and splitting impulses. The impulses do not readily scale with σ_C.

Figure 19 plots the detected collapse impulse as a function of the maximum radial bubble dimension, $r_{b,M}/r_C$. Also plotted are data from Oweis *et al.* (2004)

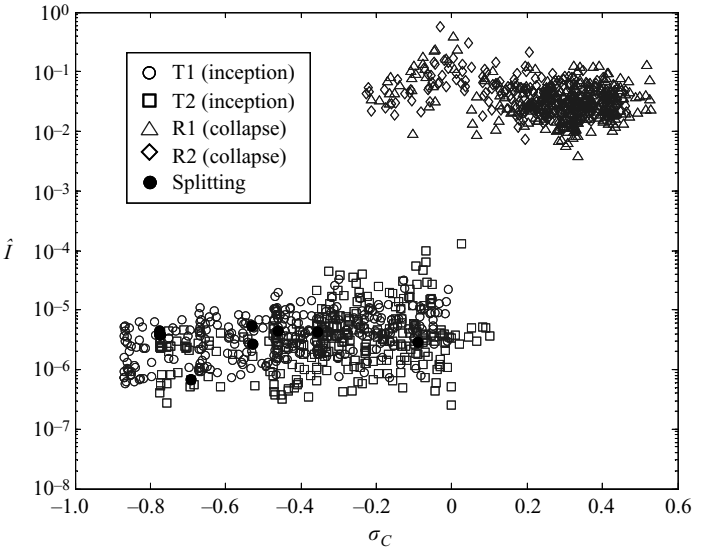

FIGURE 18. The dimensionless acoustic impulse, $\hat{I} = I_m r_H / (\frac{1}{3}\rho c \Delta P_C r_{b,M}^3 \theta)^{1/2}$, measured during inception, splitting and collapsing of the cavitation bubbles as a function of the cavitation number at the vortex core; inception noise of T1 (○), inception noise of T2 (□), collapse noise of R1 (△), collapse noise of R2 (◇), splitting noise of T1 and T2 (●); $\eta_R = 1$, $\theta = 10$ ns.

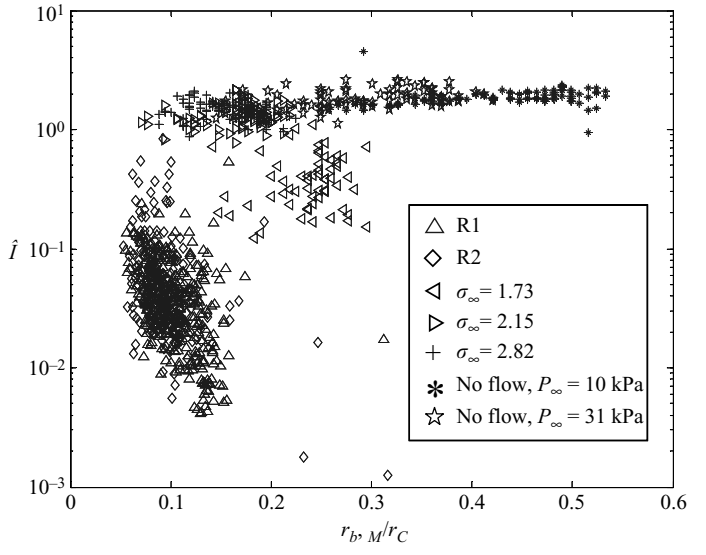

FIGURE 19. The dimensionless acoustic impulse measured during bubble collapse as a function of the dimensionless maximum bubble radius; collapse noise of R1 (△), collapse noise of R2 (◇). The data from Oweis *et al.* (2004) are also shown; laser bubble collapse without flow [$P_\infty = 10$ kPa (*), and 31 kPa (☆)]; bubbles formed in the core of the vortex $\sigma_\infty = 1.73$ (◁), $\sigma_\infty = 2.15$ (▷), $\sigma_\infty = 2.82$ (+).

for the collapse of laser-induced bubbles in a vortex, and bubbles in quiescent flow. The spherical bubbles produced in quiescent liquid produced impulses of the order of 1, implying that these bubbles converted the highest fraction of their potential

mechanical energy to radiated acoustic energy. Oweis *et al.* (2004) produced large bubbles in the vortex by explosive growth of the laser-induced bubble. (Note that the laser energy was sufficiently high to produce a vapour bubble even when the vortex core pressure was greater than vapour pressure). The resulting bubbles that were slightly deformed from a spherical shape ($\sigma_\infty = 2.15$ and 2.82) produced similar impulses. Laser-induced bubbles that were more elongated along the vortex core ($\sigma_\infty = 1.73$) had lower impulses of the order of 0.1 to 1. (The radii of these bubbles were the equivalent spherical radii.) The highest impulses observed in the present study were also of this order for bubbles with the smallest axial diameter bubbles. Larger bubbles on average yielded impulses over an order of magnitude lower, usually between 0.1 and 0.01. These data suggest that the collapse of larger, elongated bubbles is less coherent and leads to lower magnitudes of volume accelerations and hence noise emission. If the data in figure 19 were scaled with the maximum volume of the highly elongated bubble, the acoustic impulses would decrease even further relative to the near spherical bubbles.

5. Discussion and conclusion

The growth, splitting and collapse of single vortex cavitation bubbles were examined. And, these processes were related to the noise emitted by the bubble. The radius of the elongated cavitation bubbles was a fraction (<12 %) of the non-cavitating core radius, while the bubbles could grow to large aspect ratios, with values larger than 50. The axial growth rates of the bubbles were scaled with the vortex core pressure, and were larger in magnitude near inception and the final collapse. Bubble splitting was on average associated with the start of bubble collapse.

The properties of the line vortex strongly determine the shape and dynamics of the bubble, although non-cavitating vortex properties (i.e. the vortex strength and core radius) and the cavitation numbers were not sufficient to collapse the data relating to the bubble dimensions and dynamics. Instead, modest variations in the vortex properties resulted in significantly changed bubble dynamics. A two-dimensional model of the vortex cavitation bubble suggests that the final radius of the elongated bubble may take on a range of values for a given set of initial conditions, depending on the final value of the local tangential velocity near the bubble surface. Consequently, the detailed, three-dimensional process of the bubble growth may have a significant influence on the final bubble shape. Thus, the traditional scaling variables of vortex cavitation (e.g. Γ_O, r_C, σ_C, and the nucleus critical pressure) may be used to scale inception of vortex cavitation, but are insufficient to scale the developed vortex cavitation.

The noise produced by bubble growth, splitting, and collapse was examined. The noise resulting from bubble growth was measured when very small nuclei convected into a region of high liquid tension before inception. In these cases, the rapid rate of volume acceleration produced an audible pulse. Conversely, larger nuclei would begin to grow as soon as they were exposed to any tension, resulting in a reduced rate of volume acceleration. The magnitude of the noise detected during growth and splitting was similar, although the detection of splitting noise was not common. The impulse produced upon collapse was typically four to five orders of magnitude larger compared to the growth and splitting noise. The difference in noise produced by the growth of large and small nuclei illustrate the significant influence that 'water quality' can play in the scaling of vortex cavitation.

When scaling the collapse noise, only a portion of the collapsing bubble volume will contribute to the production of an acoustic pulse, making scaling with the entire bubble volume inappropriate. Moreover, the acoustic impulse produced by the collapse of deformed cavitation bubbles is still significantly lower than the impulse produced by the collapse of a spherical bubble of equivalent volume experiencing the same external driving pressure. The collapse noise did not scale with the local cavitation number. However, smaller bubbles produced relatively larger impulses, since these bubbles retained a shape that was closer to a sphere.

In conclusion, (i) the inception and dynamics of elongated vortex cavitation bubbles is a complex phenomenon that does not simply scale with the non-cavitating vortex properties and cavitation number. Instead, the detailed processes of the initial bubble growth can influence the dimensions of the elongated bubble. (ii) The detailed processes of bubble inception, splitting and collapse all influence the potential of the bubble to create an acoustic pulse (or pulses), and these processes can be influenced by the original nuclei size and the time–pressure history that the bubble experiences. The acoustic impulses did not scale with the conventional parameters, such as the local cavitation number during collapse and bubble maximum volume. This makes it difficult to derive universal relationships for the prediction and scaling of vortex cavitation noise.

This work was supported by a grant from the Office of Naval Research under Contract N00014-03-1-0430, Dr K.-H. Kim, program manager.

REFERENCES

Arndt, R. 2002 Cavitation in vortical flow. *Annu. Rev. Fluid Mech.* **34**, 143–175.

Arndt, R. & Keller, A. 1992 Water quality effects on cavitation inception in a trailing vortex. *J. Fluids Engng* **114**, 430–438.

Arndt, R. & Maines, B. 2000 Nucleation and bubble dynamics in vortical flows. *J. Fluids Engng* **122**, 488–493.

Astolfi, J. A., Fruman, D. H. & Billard, J. Y. 1999 A model for tip vortex roll-up in the near field region of three-dimensional foils and the prediction of cavitation onset. *Eur. J. Mech./*B *Fluids* **18**, 757–775.

Belahadji, B., Franc, J. P. & Michel, J. M. 1995 Cavitation in the rotational structures of a turbulent wake. *J. Fluid Mech.* **287**, 383–403.

Brennen, C. E. 1995 *Cavitation and Bubble Dynamics*. Oxford University Press.

Brennen, C. E. 2002 Fission of collapsing cavitation bubbles. *J. Fluid Mech.* **472**, 153–166.

Buogo, S. & Cannelli, G. B. 2002 Implosion of an underwater spark-generated bubble and acoustic energy evaluation using the Rayleigh model. *J. Acoust. Soc. Am.* **111**, 2594–2600.

Ceccio, S. L. & Brennen, C. E. 1991 Observations of the dynamics and acoustics of travelling bubble cavitation. *J. Fluid Mech.* **233**, 633–660.

Choi, J.-K. & Chahine, G. L. 2004 Noise due to extreme bubble deformation near inception of tip vortex cavitation. *Phys. Fluids* **16**(7), 2411–2418.

Darmofal, D. L., Khan, R., Greitzer, E. M. & Tan, C. S. 2001 Vortex core behaviour in confined and unconfined geometries: a quasi-one-dimensional model. *J. Fluid Mech.* **449**, 61–84.

Gopalan, S., Katz, J. & Knio, O. 1999 The flow structure in the near field of jets and its effect on cavitation inception. *J. Fluid Mech.* **398**, 1–43.

Hsiao, C.-T. & Chahine, G. L. 2005 Scaling of tip vortex cavitation inception noise with a bubble dynamics model accounting for nuclei size distribution. *J. Fluids Engng* **127**, 55–65.

Kuhn de Chizelle, Y., Ceccio, S. L. & Brennen, C. E. 1995 Observations and scaling of travelling bubble cavitation. *J. Fluid Mech.* **293**, 99–126.

Kumar, S. & Brennen, C. E. 1993 A study of pressure pulse generated by travelling bubble cavitation. *J. Fluid Mech.* **255**, 541–564.

Leighton, T. G., Ho, W. L. & Flaxman, R. 1997 Sonoluminescence from the unstable collapse of a conical bubble. *Ultrasonics* **35**, 399–405.

Li, C. I. & Ceccio, S. L. 1996 Interaction of single travelling bubbles with the boundary layer and attached cavitation. *J. Fluid Mech.* **322**, 329–353.

Maines, B. & Arndt, R. 1997 Tip vortex formation and cavitation. *J. Fluids Engng* **119**, 413–419.

O'hern, T. J. 1990 An experimental investigation of turbulent shear flow cavitation. *J. Fluid Mech.* **215**, 365–391.

Oweis, G. F. & Ceccio, S. L. 2005 Instantaneous and time-averaged flow fields of multiple vortices in the tip region of a ducted propulsor. *Exps. Fluids* **38**, 615–636.

Oweis, G. F., Choi, J. & Ceccio, S. L. 2004 Dynamics and noise emission of laser induced cavitation bubbles in a vortical flow field. *J. Acoust. Soc. Am.* **115**, 1049–1058.

Oweis, G. F., Hout, I. E., Iyer, C., Tryggvason, G. & Ceccio, S. L. 2005 Capture and inception of bubbles near line vortices. *Phys. Fluids* **17**, 22 105–22 118.

Tomita, Y., Tsubota, M. & Annaka, N. 2003 Energy evaluation of cavitation bubble generation and shock wave emission by laser focusing in liquid nitrogen. *J. Appl. Phys.* **93**, 3039–3048.

Vogel, A. & Lauterborn, W. 1988 Acoustic transient generation by laser-produced cavitation bubbles near solid boundaries. *J. Acoust. Soc. Am.* **84**, 719–731.